The Cryosphere Discuss., https://doi.org/10.5194/tc-2017-241
Manuscript under review for journal The Cryosphere
Discussion started: 2 January 2018

The Cryosphere Discussions

Basal drag of Fleming Glacier, Antarctica, Part A: sensitivity of inversion to temperature and bedrock uncertainty

Chen Zhao[1], Rupert M. Gladstone[2], Roland C. Warner[3], Matt A. King[1], Thomas Zwinger[4]

[1] School of Land and Food, University of Tasmania, Hobart, Australia
[2] Arctic Centre, University of Lapland, Rovaniemi, Finland
[3] Antarctic Climate and Ecosystems Cooperative Research Centre, University of Tasmania, Hobart, Australia
[4] CSC-IT Center for Science Ltd., Espoo, Finland

Abstract

Many glaciers in West Antarctica and the Antarctic Peninsula are now rapidly losing ice mass. Understanding of the dynamics of these fast-flowing glaciers, and their potential future behavior, can be improved through ice sheet modeling studies. Inverse methods are commonly used in ice sheet models to infer the basal shear stress, which has a large effect on the basal velocity and internal ice deformation. Here we use the full-Stokes Elmer/Ice model to simulate the Wordie Ice Shelf-Fleming Glacier system in the southern Antarctic Peninsula. With a control inverse method, we model the basal drag from the surface velocities observed in 2008. We propose a three-cycle spin-up scheme to remove the influence of initial temperature field on the final inversion. This is particularly important for glaciers with significant temperature-dependent internal deformation. We find that the Fleming Glacier has strong, temperature-dependent, deformational flow in the fast-flowing regions. Sensitivity tests using various bed elevation datasets and ice front boundary conditions demonstrate the importance of high-accuracy ice thickness/bed geometry data and precise location of the ice front boundary.

1 Introduction

In response to rapid changes in both atmosphere and ocean, glaciers in West Antarctica (WA) and the Antarctic Peninsula (AP) have undergone rapid dynamic thinning and ice discharge over recent decades, which has led to a significant contribution to global sea level rise (Cook et al., 2016; Gardner et al., 2017; Wouters et al., 2015). Understanding the underlying processes, especially for fast-flowing outlet glaciers, is crucial to improve modeling of ice dynamics and enable reliable predictions of contributions to sea level change.

The high velocities of the fast-flowing outlet glaciers are determined by both internal ice deformation and ice sliding at the bed. Deformation is strongly dependent on gravitational driving stress, englacial temperature, the development of anisotropic structure at the grain scale in polycrystalline ice (Gagliardini et al., 2009) and larger scale weakening from fractures (Borstad et al., 2013). Basal sliding is strongly dependent on the gravitational driving stress, bedrock topography and the basal slipperiness, which in turn is affected by the roughness of the bed, the presence of deformable till, or the basal hydrology. Therefore, one of the keys to modeling fast-flowing glaciers is accurate knowledge of the basal conditions: the bedrock topography and the basal slipperiness (Gillet-Chaulet et al., 2016; Schäfer et al., 2012). Inverse methods are commonly used in ice sheet models to infer the basal shear stress and basal velocities from the glacier topography and observed surface velocities (Gillet-Chaulet et al., 2016; Gladstone et al., 2014; Morlighem et al., 2010).

However, poorly constrained quantities, like the basal topography, and the distribution of internal temperature, have provided major challenges for modeling the basal shear stress, especially for small-scale glaciers. In a study carried out on a fast-flowing outlet glacier draining from the Vestfonna ice cap in the Arctic (Schäfer et al., 2014; Schäfer et al., 2012), it was found that the inverse methods did not depend strongly on the mesh resolution or uncertainties in the topographic and velocity data. The impact of ice temperature on ice internal deformation was relatively small compared to the important role of friction heating at the bed on the basal sliding (Schäfer et al., 2014; Schäfer et al., 2012). However, no generalization on these findings to Antarctic outlet glaciers has been investigated. The motivation of this paper is twofold: to test the sensitivity of inversion methods to basal geometry and englacial temperature distribution for a different outlet glacier system, and to determine a robust basal shear stress pattern for the Fleming Glacier, located in the southern AP, in 2008.

The Wordie Ice Shelf (WIS) (Fig. 1b) in the southern AP has experienced ongoing retreat and collapse since 1966, with its almost-complete disappearance by 2008 (Cook and Vaughan, 2010; Zhao et al., 2017). The Fleming Glacier (FGL) (Fig. 1b), as the main tributary glacier, has shown a rapid increase in surface-lowering rates (Zhao et al., 2017), and the largest velocity changes across the whole Antarctic over 2008-2015 (Walker and Gardner, 2017). In this study, we employed the Elmer/Ice code (Gagliardini et al., 2013), a three-dimensional (3D), finite element, full-Stokes ice sheet model, to invert the basal drag coefficients over the whole WIS-FGL system in a parallel computing environment.

Here, we deduce the distribution of basal shear stress using a control inverse method to assess its sensitivity to bedrock topographies, assumptions about the initial temperature distribution and other constraint parameters in the model. We introduce the data in Sect. 2, present the ice sheet model, spin-up scheme and experiment design in Sect. 3, and discuss the results in Sect. 4 before we give the conclusions in Sect. 5.

2 Data

2.1 Surface elevation data in 2008

The surface topography in 2008 (Fig. 2a) is combined from two SPOT DEM products acquired on 21st Feb, 2007 (resolution: 240 m) and 10th Jan, 2008 (resolution: 40 m) (Korona et al., 2009) and an ASTER DEM product ranging from 2000 to 2009 (resolution: 100m) (Cook et al., 2012). Here we apply the SPOT DEM precision quality masks on the raw data to extract the DEM data with correlation scores from 20% to 100%. Areas with low correlation scores were filled with the ASTER DEM data. To remove noise from the DEM data, the combined DEM (resolution: 40 m) is resampled to 400 m with a median filter and a window size of 10×10 pixels. The EGM96 geoid (Lemoine et al., 1998) is used to convert from the EGM96 Geoid values to WGS84 ellipsoidal heights. We extract a median value of 15 m for the DEM data over Marguerite Bay (Fig. 1a) as the mean local sea level in the ellipsoid frame.

2.2 Bed elevation data

The bed topography plays a very important role in the basal sliding and distribution of fast-flowing ice (De Rydt et al., 2013). However, high-resolution observations of bedrock elevation for this region are still not available. To explore the sensitivity of the basal shear stress distribution to the uncertainty in the bedrock topography, we adopt three basal topographies. The first is from the Bedmap2 dataset (Fretwell et al., 2013) with a resolution of 1 km (hereafter bed_bm; Fig. 2b). The other two are derived using the equations below:

$$bed\_zc = S_{2008} - H_{mc} \quad (1)$$

$$bed\_mc = S_{bm} - H_{mc} \quad (2)$$

The Cryosphere Discuss., https://doi.org/10.5194/tc-2017-241
Manuscript under review for journal The Cryosphere
Discussion started: 2 January 2018

where S_{2008} is the surface DEM in 2008 mentioned in Sec. 2.1, S_{bm} is the surface elevation data from Bedmap2 (Fretwell et al., 2013), and H_{mc} (where "mc" refers to "mass conservation") is the ice thickness data with a resolution of 450 m combined from three sources shown in Figs. 2e: data for the yellow area is computed from the Center for Remote Sensing of Ice Sheets (CReSIS) ice thickness measurements using a mass conservation method (Morlighem et al., 2011; Morlighem et al., 2013); data for the grey area is interpolated from Bedmap2 (Fretwell et al., 2013); while in the red area thickness is interpolated from CReSIS and Bedmap2 data. The yellow area is the Fleming Glacier system with ice velocity >100 m yr^{-1}. The uncertainty of H_{mc} (Fig. 2f) ranges from 10 m to 108 m. For the calculation of H_{mc}, we assume the ice elevation changes over 2002 to 2008 (Zhao et al., 2017) were small compared to the uncertainty in ice thickness (Fig. 2f). Both bed_mc (Fig. 2c) and bed_zc (Fig. 2d) have a higher resolution of 450 m while bed_bm (Fig. 2b) has a resolution of 1 km. The uncertainty of bed_bm for the fast-flowing regions of the Fleming Glacier (yellow and red area in Fig. 2e) ranges from 151 m to 322 m, while the uncertainty of bed_mc and bed_zc ranges from 10 m to 108 m (from uncertainties in H_{mc}).

The bed topography data (Fig. 2b) indicates two basins featuring retrograde slopes underneath the Fleming Glacier. The region further upstream (hereafter "FG upstream basin") has a steeper retrograde slope than the one close to the grounding line of those basins (hereafter "FG downstream basin"). For the FG downstream basin, elevation differences between bed_bm and the other two datasets (Figs 2c, 2d) show that bed_bm has a steeper retrograde slope. The sensitivity of basal shear stress to the three bed datasets is discussed in Sect. 4.2.

2.3 Surface velocity data in 2008

The surface velocity data used for 2008 (Fig. 1b) were obtained from MEaSUREs InSAR-based Antarctic ice velocity (from the fall 2007 and/or 2008) produced by Rignot et al. (2011b) (version 1.0) with a resolution of 900 m and with uncertainties ranging from 4 m yr^{-1} to 8 m yr^{-1} over the study area. For the regions without data (grey area in Fig. 1b), we prescribe the surface speed to be 0. We do not use the finer (450 m) resolution velocity here since the coarser (900 m) resolution data have been subjected to some post-processing, including smoothing and error corrections.

3 Method

All the simulations are carried out using the Elmer/Ice model (Gagliardini et al., 2013). These simulations are used to solve the ice momentum balance equations with a control inverse method to determine basal drag, and the steady state heat equation for the ice temperature distribution. The ice rheology is given by Glen's flow relation (Glen, 1955) with viscosity computed using an overall flow enhancement factor, $\boldsymbol{E}$, and a function of the ice temperature relative to the pressure melting point according to the Arrhenius Law (Gagliardini et al., 2013). Table 1 lists the parameters used in this study.

3.1 Mesh generation and refinement

We used GMSH (Geuzaine and Remacle, 2009) to generate the 2-D horizontal footprint mesh with the boundary defined from the grounding line data in 1996 (Rignot et al., 2011a) and the catchment boundary of the feeding glacier system (Cook et al., 2014), with the assumption that the ice front position in 2008 was coincident with the grounding line position in 1996 (Rignot et al., 2011a).

To reduce the computational cost without reducing the accuracy, we refined the mesh using the anisotropic mesh adaptation software YAMS (Frey and Alauzet, 2005) using the local Hessian matrix (second order derivatives) of the surface velocity data in 2008 from Rignot et al. (2011b). The resulting mesh is shown in Fig. 3 with the minimum and maximum element

The Cryosphere Discuss., https://doi.org/10.5194/tc-2017-241
Manuscript under review for journal The Cryosphere
Discussion started: 2 January 2018

sizes of approximately 250 m and 4 km, respectively. The 2-D mesh is then vertically extruded using 10 equally spaced, terrain following layers. Sensitivity tests have been done on the Vestfonna ice cap (Schäfer et al., 2014; Schäfer et al., 2012) to prove the robustness of inverse simulations to the vertical mesh resolution. It would be useful to know whether the WIS-FGL system shows same robustness to the vertical resolution, but this is beyond the scope of current study.

3.2 Boundary Conditions

For transient simulations (surface relaxation, section 3.3), the stress-free upper surface is allowed to evolve freely, with a minimum imposed ice thickness of 10 m over otherwise ice-free terrain. For inverse and temperature simulations, the upper surface height and temperature are fixed.

At the ice front, the normal component of the stress where the ice is below sea level is equal to the hydrostatic water pressure exerted by the ocean. The uncertainties of ice thickness and bedrock topography, the low accuracy of ice front and grounding line locations, and the possible buttressing on the ice front by partly detached icebergs and ice mélange (see Fig. 1c) would affect the calculation of ocean forcing there. Accordingly, we will discuss the sensitivity to the ice front boundary condition in Sect. 4.3. On the lateral boundary, which falls within glaciated regions, the normal component of the stress vector is set equal to the ice pressure exerted by the neighboring glacier ice while the tangential velocity is assumed to be zero.

The bedrock is regarded as rigid, impenetrable, and temporarily fixed in all simulations. The present-day solid Earth deformation rate in the Fleming glacier region (Zhao et al., 2017) is negligible compared to the uncertainty of the bedrock data. So, the normal basal velocity is assumed to be zero here. The sliding relation relates the basal sliding velocity u_b to basal shear stress τ_b. Here, a simple linear sliding law is applied on the bottom surface:

$$\tau_b = Cu_b \tag{3}$$

where C is a basal sliding coefficient. During the initial surface relaxation, and at the start of the inversion, C is initialized to a constant value of 10^{-4} MPa m^{-1} yr, which is replaced with the inverted C in following steps.

The surface temperature is defined by the yearly averaged surface temperature over 1979-2014 computed from the regional atmospheric climate model RACMO2.3/ANT27 (van Wessem et al., 2014). The geothermal heat flux (GHF) at the bed is obtained from Fox Maule et al. (2005) using input data from SeaRISE project, and the GHF is interpolated with bilinear interpolation method from the standard 5 km grid onto the anisotropic mesh. A basal heat flux boundary condition combining GHF and basal friction heating is imposed for temperature simulations.

3.3 Surface relaxation

There may be non-physical spikes in the initial surface geometry, caused for example by observational uncertainties of the surface or bedrock data and/or by the resolution discrepancy between mesh and geometry data. To reduce these features, we relaxed the free surface of this domain during a short transient simulation of 0.2 yr length with a timestep of 0.01 yr.

3.4 Inversion for basal shear stress

After the surface relaxation, we used the control inverse method (MacAyeal, 1993; Morlighem et al., 2010) implemented in Elmer/Ice (Gagliardini et al., 2013; Gillet-Chaulet et al., 2012) to constrain the basal sliding coefficient C in Eq. 3. To avoid non-physical negative

The Cryosphere Discuss., https://doi.org/10.5194/tc-2017-241
Manuscript under review for journal The Cryosphere
Discussion started: 2 January 2018

values, we used a logarithmic representation of the basal drag coefficient, $C = 10^{\beta}$, where β can take any real value.

The inverse method is based on adjusting the spatial distribution of the basal drag coefficient to minimize a cost function that represents the mismatch between the simulated and observed surface velocities. To avoid over-fitting of the inversion solution to non-physical noise in the observations, a regularization term is added to the cost function as:

$$J_{tot} = J_0 + \lambda J_{reg} \tag{4}$$

where $\boldsymbol{J_0}$ represents the square of the magnitude of the mismatch between the simulated and observed surface velocities, J_{reg} is the regularization term imposing a cost on spatial variations in the control parameter β, λ is a positive regularization weighting parameter, and $\boldsymbol{J_{tot}}$ is the total cost. Thus, the minimum of this cost function is no longer the best fit to observation but a compromise between fit to observations and smoothness in β. An L-curve analysis (Hansen, 2001) has been carried out for inversions in the current study to find the optimal λ by plotting the term J_{reg} as the function of J_0. The optimal value of 10^8 is chosen for λ to minimize $\boldsymbol{J_0}$.

With $\lambda = 10^8$, we compute the total cost $\boldsymbol{J_{tot}}$ with different values of flow enhancement factor $\boldsymbol{E}$ (0.7, 1, 2.5, 5, 10). It is found that inversions with smaller $\boldsymbol{E}$ gave a better-simulated surface velocity for slow ice-flow regions while greater $\boldsymbol{E}$ gave a better velocity for fast ice-flow regions. The optimal value of $\boldsymbol{E} = 2.5$ is chosen for the current study.

3.5 Steady-state temperature simulations

In the absence of a known englacial temperature distribution for the Fleming Glacier system, the steady state ice temperature is solved for use in the inversion process. The ice velocity and geometry are held constant for this simulation. Steady-state temperature simulation for a non-steady-state glacier system will result in the estimations of the temperature that deviate from actuality. However, similar experiments on the Greenland Ice Sheet indicated that the simulated steady-state temperature field could present a reasonable thermal regime for calculation of basal conditions (Seroussi et al., 2013). Heat sources and internal energy transfer determine the temperature distribution within the ice. The heat transfer equation is solved using an iterative method as described in Gagliardini et al. (2013).

3.6 Experiment design

The four-step spin-up scheme (Gladstone et al., 2014) has been adopted in inverse modeling using Elmer/Ice (Gong et al., 2016), without testing the effect of initial temperature assumption on the inversion results. To explore the sensitivity of inverse modeling to initial temperature assumptions, we proposed a spin-up scheme with more cycles (three cycles in this study as presented in Fig. 4). For each cycle, we followed the spin-up scheme of Gladstone et al. (2014):

1. surface relaxation;
2. inversion for basal friction coefficient using the relaxed surface geometry;
3. a steady state temperature simulation using the simulated velocity from that inversion;
4. another inversion with simulated steady-state temperature.

The surface relaxation for each cycle starts from the same initial geometry described in Sect. 3.3. For cycle 1, the surface relaxation and first inversion are implemented with an initial temperature assumption (described below) and uniform basal drag coefficient. For cycle 2 and 3, the surface relaxation and inversion are implemented with simulated steady-state temperature and basal drag coefficient $\boldsymbol{C}$ from the final state of the previous cycle.

To explore the sensitivity of inverse methods to temperature distribution, basal topography, and the ice front boundary conditions, we carried out the experiments summarized in Table 2.

Initial temperature used in the surface relaxation would affect the modelled ice deformation and ice velocity field, especially for fast-flowing regions, and consequently lead to a difference in the relaxed upper surface, which might affect the subsequent inversion process. To explore the impact of initial temperature on inversion results with three-cycle spin-up scheme, we proposed experiments with different initial temperature assumptions for the surface relaxation and initial inversion in Cycle 1. TEMP1: a uniform temperature of -20 ℃; TEMP2: a uniform temperature of -5 ℃; CONTROL: a linearly increasing temperature from the upper surface values (see also Sect. 3.2) to the pressure melting temperature at the bed. To test the sensitivity of basal drag to the relaxed geometry, we also added another experiment "TEMP3": surface relaxation in the first cycle using the linear temperature, followed by inversion with a uniform temperature of -20 ℃.

As described in Sec. 2.2, we generated three different bed topography datasets to explore the sensitivity of the inverse modelling. The three-cycle spin-up scheme is carried out for each bed dataset using the linear (described above) initial temperature distribution. These experiments are referred to as CONTROL, BEDZC, and BEDMC (Table 2).

Uncertainties from the ice thickness and bedrock datasets may have a significant effect on the pressure boundary condition applied to the ice front, which balances the normal stress in the ice against the ocean water pressure. In view of the ice thickness uncertainty (ranging from 10 m to 100 m) and hence bedrock depth around the grounding line, and given the possibility of increased additional pressure due to floating icebergs and ice mélange as indicated in Fig. 1c, we vary this boundary condition by varying the sea level used to calculate pressure. This approach directly represents some small uncertainty in the exact sea level itself, but is also a proxy for pressure errors due to thickness uncertainty and mélange backstress. We adjust the sea level by 10 m from hydraulic equilibrium to test the sensitivity of the inverse modeling to the ice front boundary condition. Firstly, we assume an ocean pressure at the ice front computed using the sea level mentioned in Sec. 2.1. We further simulate two alternative scenarios for the sea level used in the simulations: IFBC1 with sea level of 5 m and IFBC2 with sea level of 25 m. Another extreme scenario (IFBC3, Table 2) is adopted here by setting the ice front pressure to:

$$P_i(z) = \rho_i g(z_s - z) \tag{5}$$

where $P_i(z)$ is the pressure at the ice front as a function of height z, ρ_i is ice density (Table 1), g is the gravitational constant (Table 1), and z_s is the height of ice upper surface at the ice front. This is the pressure that would be imposed by a neighboring glacier, and imposes zero normal strain rate at the ice front. The ice surface elevation z_s at the front is ~115 m. The total vertically integrated pressure imposed by this condition is equivalent to a sea level of ~60 m, though the vertical distribution of pressure is different to an ocean pressure condition.

4 Results

The main focus of the current study is the sensitivity of the inversion to the three factors: temperature initialization, bed topography and ice front stress balance. The evaluation criteria are the robustness of simulated basal drag coefficient distribution and the mismatch between the simulated and observed surface velocities.

4.1 Sensitivity to initial temperature

We present the results of the four TEMP experiments (Sect. 3.7, Table 2) for the WIS-FGL system. All those experiments showed that the absolute difference between the relaxed and the observed surface was < 30 m, smaller than the ice thickness uncertainty (> 50 m) used in this study. However, we think some of the systematic changes generated by surface relaxation are not correcting real errors in the surface topography data, as discussed later in Sect. 4.3. After the first cycle (left column, Fig. 5), results showed different patterns of basal drag coefficient for each experiment, especially in the fast-flowing regions with surface velocity higher than 1000 m/yr (yellow contour in Fig. 5). The basal drag from TEMP2 (Fig. 5d) and CONTROL (Fig. 5g) share a very similar rib-like pattern around the ice front, some isolated sticky spots and another rib close to the yellow contour in the fast flow regions (> 1000 m yr^{-1}), but the TEMP1 (Fig. 5a) and TEMP3 (Fig. 5j) display different patterns, indicating dependence on the initial temperature assumption. This is in contrast to a similar inverse study on the Vestfonna ice cap (Schäfer et al., 2012), which showed little impact of temperature distribution on the basal sliding coefficient. That was due to a low contribution of ice deformation to ice motion compared to the basal sliding (Schäfer et al., 2012). We return to this contrast after considering the effect of the second and third cycles of our spin-up.

To remove the dependence on initial temperature and achieve a consistent equilibrium thermal regime with respect to the given slip coefficient distribution for surface relaxation, we carried out the second cycle shown in Fig. 4. The basal drag coefficient from the final step of Cycle 2 (the middle column in Fig. 5) shows greater similarity across all the temperature experiments. However, the sticky points upstream of the grounding line in the downstream basin show a trend of decreasing and disappearing from the first cycle (left column of Fig 5) to the second cycle (middle column of Fig 5) for experiments CONTROL" and TEMP2. Therefore, a third cycle was implemented for all temperature assumptions. After the third cycle, all the scenarios depicted a similar basal drag coefficient pattern (right column in Fig. 5). The differences between the simulated and observed surface speed for the above experiments (Fig. 6) also prove that the three-cycle scheme could provide relatively robust inversion results with little sensitivity to the initial temperature. Considering the linear temperature is likely closer to a realistic temperature distribution, we adopted the scenario with initial linear temperature for the experiments described hereafter.

The present study is focused on exploring the effects of uncertainties and their control, and dynamics of the FGL system will be discussed in more detail in a companion paper (Zhao et al., companion paper). However, a few comments are in order regarding the contrast with the previous study on the Vestfonna ice cap. The low impact of temperature distribution on the basal sliding in that study was due to a lower contribution of ice deformation to ice motion compared to the basal sliding (Schäfer et al., 2012). Internal ice deformation, and hence temperature, may be especially important for the WIS-FGL system due to steep surface slopes and corresponding high driving stresses in the region between the downstream and upstream basins (Fig. 7a). The patterns of basal drag coefficient (right column of Fig. 5) all indicate substantial differences in basal drag over the fast flowing part of the FGL. For example, in the region flowing at over 1000 m yr^{-1} (inside the yellow contour), we see very low drag over the downstream basin, but higher drag coefficients over the upstream bedrock high, and in a narrow band along the ice front. The nature of the basal shear stress is further complicated by substantial variations in the contribution of basal sliding velocity and of vertical shear deformation to the flow. A comparison between the simulated basal and surface velocities (Fig. 7b) shows that internal deformation dominates the ice dynamics in some of the fast-flowing regions. This alone would suggest a high sensitivity of modelled sliding velocity and basal drag to the englacial temperature.

The three-cycle iterative spin-up scheme is suggested as an effective set-up for inverse modeling of fast-flowing glaciers that have high surface slopes and vertical shear strain rates and therefore are sensitive to the internal vertical ice temperature field. In other cases, the inversion process is not so heavily dependent on the temperature field, for example for reproducing the shear margins of the outlet glacier of Basin 3 on Austfonna ice cap, Svalbard (Gladstone et al., 2014).

4.2 Sensitivity to bedrock topography

Figure 8 summarizes results from the three experiments using different bed topographies (Sect. 3.7, Table 2). The 2008 ice velocity contours are added as visual references for comparing the basal drag coefficient patterns in the regions of fast flow, since the largest observed ice velocity changes occurred in fast outlet flow regions (Mouginot et al., 2014; Walker and Gardner, 2017). As shown in Fig. 8, the simulated basal friction coefficient ***C*** varies with bedrock geometry and its distribution shows greater similarity between BEDZC and BEDMC. CONTROL (using "bed_bm"; Fig. 8a) shows slightly smaller basal drag coefficients than BEDMC (Fig. 8b) and BEDZC (Fig. 8c) in the fast-flowing region (>1500 m yr^{-1}, cyan contour in Fig. 8) and the pattern in the region between the yellow and cyan contours also differs in the CONTROL case, which might be caused by the deeper bedrock of bed_bm in the FG downstream basin (Fig. 8g), compared to the other two datasets (Figs. 8h, 8i). However, all three cases indicate similar regions with low basal drag coefficient in fast flow regions (>1500 m yr^{-1}, cyan contour in Fig. 8), which is consistent with the boundary of the FG downstream basin.

The simulated surface velocities from BEDZC (Fig. 8e) and BEDMC (Fig. 8f) match the observed surface velocities better than those from CONTROL (Fig. 8d) in the regions around the ice front/grounding line and more broadly for velocity exceeding 1000 m yr^{-1}. The deeper retrograde bed in the CONTROL simulation may indicate increased vulnerability to marine ice sheet instability, and more overestimation of surface velocity is found around the grounding line (Fig. 8d). One possible cause of the different basal shear stress in these inversions might be the increased slope caused by the surface relaxation. However, we find the inversion process is not sensitive to the surface relaxation, and this is further discussed in Sect. 4.3. It means a high-accuracy bedrock topography data is very important for inverse modeling owing to the fact that the bedrock resolution around the grounding line determines the ice dynamics (Durand et al., 2011). Comparison of the distribution of velocity mismatch and ***C*** between BEDZC and BEDMC does not provide a clear insight into which is the best basal geometry for modeling this system. We compute the root mean square errors (RMSE) of the velocity mismatch for the regions with velocity >1500 m yr^{-1}, and find the RMSE of BEDMC is marginally larger than the RMSE of BEDZC. While both use the ice thickness extracted using the mass conservation mechanism, BEDZC maintains better consistency with the surface elevation data used in current study than BEDMC. Therefore, bed_zc is suggested as the best current bedrock elevation data for further ice sheet modeling of the WIS-FGL system.

4.3 Sensitivity to ice front boundary condition

All the inversions so far feature both a band of high basal drag near the ice front of the Fleming Glacier (right column of Fig. 5 and left column of Fig. 8) and a similar localized overestimate of upper surface velocities at the ice front (right column of Fig. 6 and middle column of Fig. 8). We now consider causes for possible uncertainties about the force applied to the ice front, and whether the high friction near the ice front is likely to be a feature of the real system or a compensating response to incorrect boundary forcing by the inversion process. These possible causes include uncertainty in local bedrock elevation, uncertainty in observed sea level, uncertainty in exact ice front position and grounding line position, uncertainty in surface velocity, and uncertainty in potential backstress due to ice mélange and or grounded icebergs in contact with the ice front. The sensitivity to bedrock uncertainty has been discussed in Sec. 4.2. In our model domain we assume the 2008 grounding line is consistent with the 1996 grounding line, which has an error of several km on fast-moving ice (Rignot et al., 2011a) and might have changed since 1996. The frontal surface elevation is from the SPOT DEM data in Jan 2008, which shows the ice front position is ~1.5 km downstream of the 1996 grounding line position. Since such a narrow residual ice shelf was considered unlikely to have a major influence we constructed the model geometry to have the ice front coincide with the 1996 grounding line for simplicity, i.e. all ice is considered grounded. In this framework uncertainty about the bedrock depth at the ice front feeds in to significant uncertainty in the total restraining force from ocean pressure. Friedl et al. (2017) presented evidence that an acceleration phase occurred around March-April 2008, but we are not sure the specific month of the surface velocity data used in this study (Rignot et al., 2011b). It means the surface velocity data, which is the target to be matched by the control inverse process, might not be consistent with the DEM data used here.

To explore the influence of these different sources of uncertainty, we adopt different sea level heights within our vertical reference frame to apply a range of ocean pressures to the ice front as described in Sect. 3.6 (IFBC1-3, Table 2). A higher sea level in the ice front boundary condition imposes a higher pressure at the ice front, i.e. a higher total retarding force, and we impose these different boundary conditions as a proxy for the sources of uncertainty discussed above.

Basal drag coefficients $\boldsymbol{C}$ simulated from the IFBC experiments present different patterns around the ice front regions of the FGL (within ~1 km of the grounding line). Experiments with higher sea levels display smaller $\boldsymbol{C}$ there (Fig. 9, left column) and provide a better match between modeled and simulated surface velocities (Fig. 9, middle column). If the applied ice front boundary condition underestimates the real world forcing, the inversion process will compensate by increasing the basal drag in this region. However, the large vertical shear strain rate imposes a limit to how much increasing basal drag can reduce the surface velocity, which could explain why the mismatch between the modeled and observed velocity is still large in the narrow band near the ice front (Fig. 9, middle column). For the fast-flowing region (velocity > 1500 m a^{-1}), the decreased basal shear force from IFBC2 to IFBC3 ($\sim 1.1\times10^{11}$ N) roughly matches the increased the ice front pressure over a 6 km length of ice front ($\sim 2.8\times10^{11}$ N).

Experiment "IFBC3", with an extreme assumption of applying ice pressure corresponding to a neighbouring column of ice matching the ice front, shows very small basal drag for the ice front area around the grounding line, and also resulted in lower drag over the downstream basin (Fig. 9d). However, "IFBC3" introduces a greater mismatch to the observed surface velocities (Fig. 9h), with lower simulated velocities over a substantial region extending upstream from the ice front and greater overestimate of velocities further upstream. This is only a sensitivity test but implies a potentially suitable ice front pressure may lie between "IFBC2" and "IFBC3". This set of experiments also suggests that moderate changes influence only a limited area. It is hard to decide the best ice front boundary condition here owing to the lack of precise bedrock data (as seen above) and difficulty of estimating the additional pressure from the partly detaching icebergs and ice mélange. But it is certain that the ice front boundary conditions can have a significant effect on the inversion results near the grounding line.

The different ice front boundary conditions also lead to significant differences in the surface relaxation at the ice front, with lower sea levels leading to greater lowering and corresponding steepening of the surface adjacent to the ice front (Fig. 9, right column). The differences in surface elevation are localized to the ice front zone, with the relaxation over the rest of the domain essentially unaffected, even for the most extreme forcing. This is apparently the consequence of rapid spreading of an ice cliff over 100 m higher than the control sea level at the ice front due to its own weight. Thus, the inversions are potentially influenced both by the ice front condition directly in the overall momentum balance and also by the increased local driving stress due to this artificially steeper surface slope. The band of higher basal drag near the ice front may be partly a response to these issues. However, an additional simulation (not shown), in which a high sea level was used for the surface relaxation step and a low sea level for the inversion, gave a relaxed surface very close to observations (no steepening) and still showed the high basal friction band near the ice front. This implies that the high friction near the ice front is directly sensitive to the boundary condition at the ice front but not to associated artifacts in the surface relaxation.

At present we cannot be sure whether the high friction near the ice front is a real feature, an artifact due to errors in the ice front boundary condition, or a combination of both. However, the impact diminishes rapidly with distance inland for moderate sea level shifts, which do not affect the general pattern of basal shear stress or the quality of the velocity matching more than ~2 km upstream of the grounding line.

5 Conclusions

We have obtained a basal drag coefficient distribution for the Wordie Ice Shelf-Fleming Glacier system in 2008, using an iterative spin-up scheme of simulations, observed surface velocities and a detailed surface DEM. We explored the sensitivity of the inversion for basal drag to three inputs to the modelling process. Within the approximation of using simulated steady-state ice temperatures, we showed that three cycles of iteration removed the influence of initial englacial temperature assumptions. In contrast to the observed low sensitivity to the englacial temperature of outlet glaciers from the Vestfonna Ice Cap (Schäfer et al., 2014; Schäfer et al., 2012), the first cycle of our iterative process showed that the inferred basal stress of the Fleming Glacier system is highly sensitive to the englacial temperature distribution. This conclusion is expected to also apply to other fast-flowing glacier systems with a significant dependence on the internal deformation. For such glacier systems, a multiple-cycle spin-up scheme is likely to be necessary.

For our model of the Wordie Ice Shelf-Fleming Glacier system, our sensitivity tests to different basal elevation datasets indicate a high dependence of basal inversion on the accuracy of bed topography. The “bed_zc” bed topography, which used ice thickness determined using the mass conservation method for the fast-flowing regions, is suggested as the best current bed topography for further simulations in this region.

For the Wordie Ice Shelf-Fleming Glacier system, which we treated as grounded adjacent to the ice front, the inferred basal drag coefficient near that grounding line is sensitive to the ice front boundary condition, emphasizing the importance of the normal force on the ice front. This finding, combined with the sensitivity of surface relaxation to ice front boundary condition, implies that an accurate representation of the ice front boundary will be important for inverse modeling and transient simulations of the Wordie Ice Shelf-Fleming Glacier system.

Author Contributions

Chen Zhao and Rupert Gladstone designed the experiments together. Chen Zhao collected the datasets, ran the simulations, and drafted the paper. All authors contributed to the refinement of the experiments, the interpretation of the results and the final manuscript.

Acknowledgements

Chen Zhao is a recipient of an Australian Government Research Training Program Scholarship and Quantitative Antarctic Science Program Top-up Scholarship. Rupert Gladstone is funded by the European Union Seventh Framework Programme (FP7/2007-2013) under grant agreement number 299035 and by Academy of Finland grant number 286587. Matt A. King is a recipient of an Australian Research Council Future Fellowship (project number FT110100207) and is supported by the Australian Research Council Special Research Initiative for Antarctic Gateway Partnership (Project ID SR140300001). Thomas Zwinger’s contribution has been covered by the Academy of Finland grant number 286587. This work was supported by the Australian Government’s Business Cooperative Research Centres Programme through the Antarctic Climate and Ecosystems Cooperative Research Centre (ACE CRC). This research was undertaken with the assistance of resources and services from the National Computational Infrastructure (NCI), which is supported by the Australian Government. We thank Fabien Gillet-Chaulet for advice on implementation of the inversion.

The Cryosphere Discuss., https://doi.org/10.5194/tc-2017-241
Manuscript under review for journal The Cryosphere
Discussion started: 2 January 2018

We thank Mathieu Morlighem for the mass-conservation constrained ice thickness data. We thank E. Rignot, J. Mouginot, and B. Scheuchl for making their SAR velocities publically available. SPOT 5 images and DEMs were provided by the International Polar Year SPIRIT project (Korona et al., 2009), funded by the French Space Agency (CNES). The ASTER L1T data product was retrieved from https://lpdaac.usgs.gov/data_access/data_pool, maintained by the NASA EOSDIS Land Processes Distributed Active Archive Center (LP DAAC) at the USGS/Earth Resources Observation and Science (EROS) Center, Sioux Falls, South Dakota.

Reference

Borstad, C. P., Rignot, E., Mouginot, J., and Schodlok, M. P.: Creep deformation and buttressing capacity of damaged ice shelves: theory and application to Larsen C ice shelf, The Cryosphere, 7, 1931-1947, 2013.

Cook, A. J., Holland, P. R., Meredith, M. P., Murray, T., Luckman, A., and Vaughan, D. G.: Ocean forcing of glacier retreat in the western Antarctic Peninsula, Science, 353, 283-286, 2016.

Cook, A. J., Murray, T., Luckman, A., Vaughan, D. E., and Barrand, N. E.: A new 100-m Digital Elevation Model of the Antarctic Peninsula derived from ASTER Global DEM: methods and accuracy assessment, Earth System Science Data, 4, 129-142, 2012.

Cook, A. J., Vaughan, D., Luckman, A., and Murray, T.: A new Antarctic Peninsula glacier basin inventory and observed area changes since the 1940s, Antarctic Science, 26, 614, 2014.

Cook, A. J. and Vaughan, D. G.: Overview of areal changes of the ice shelves on the Antarctic Peninsula over the past 50 years, The Cryosphere, 4, 77-98, 2010.

De Rydt, J., Gudmundsson, G. H., Corr, H. F. J., and Christoffersen, P.: Surface undulations of Antarctic ice streams tightly controlled by bedrock topography, The Cryosphere, 7, 407-417, 2013.

Durand, G., Gagliardini, O., Favier, L., Zwinger, T., and le Meur, E.: Impact of bedrock description on modeling ice sheet dynamics, Geophysical Research Letters, 38, n/a-n/a, 2011.

Fox Maule, C., Purucker, M. E., Olsen, N., and Mosegaard, K.: Heat Flux Anomalies in Antarctica Revealed by Satellite Magnetic Data, Science, 309, 464-467, 2005.

Fretwell, P., Pritchard, H. D., Vaughan, D. G., Bamber, J. L., Barrand, N. E., Bell, R., Bianchi, C., Bingham, R. G., Blankenship, D. D., Casassa, G., Catania, G., Callens, D., Conway, H., Cook, A. J., Corr, H. F. J., Damaske, D., Damm, V., Ferraccioli, F., Forsberg, R., Fujita, S., Gim, Y., Gogineni, P., Griggs, J. A., Hindmarsh, R. C. A., Holmlund, P., Holt, J. W., Jacobel, R. W., Jenkins, A., Jokat, W., Jordan, T., King, E. C., Kohler, J., Krabill, W., Riger-Kusk, M., Langley, K. A., Leitchenkov, G., Leuschen, C., Luyendyk, B. P., Matsuoka, K., Mouginot, J., Nitsche, F. O., Nogi, Y., Nost, O. A., Popov, S. V., Rignot, E., Rippin, D. M., Rivera, A., Roberts, J., Ross, N., Siegert, M. J., Smith, A. M., Steinhage, D., Studinger, M., Sun, B., Tinto, B. K., Welch, B. C., Wilson, D., Young, D. A., Xiangbin, C., and Zirizzotti, A.: Bedmap2: improved ice bed, surface and thickness datasets for Antarctica, The Cryosphere, 7, 375-393, 2013.

Frey, P.-J. and Alauzet, F.: Anisotropic mesh adaptation for CFD computations, Computer methods in applied mechanics and engineering, 194, 5068-5082, 2005.

Friedl, P., Seehaus, T. C., Wendt, A., Braun, M. H., and Höppner, K.: Recent dynamic changes on Fleming Glacier after the disintegration of Wordie Ice Shelf, Antarctic Peninsula, The Cryosphere Discuss., 2017, 1-26, 2017.

Gagliardini, O., Gillel-Chaulet, F., and Montagnat, M.: A Review of Anisotropic Polar Ice Models : from Crystal to Ice-Sheet Flow Models, Physics of Ice Core Records II, Institute of Low Temperature Science, Hokkaido University, Sapporo, 25 Japan, 2009. 2009.

Gagliardini, O., Zwinger, T., Gillet-Chaulet, F., Durand, G., Favier, L., de Fleurian, B., Greve, R., Malinen, M., Martín, C., Råback, P., Ruokolainen, J., Sacchettini, M., Schäfer, M., Seddik, H., and Thies, J.: Capabilities and performance of Elmer/Ice, a new-generation ice sheet model, Geosci. Model Dev., 6, 1299-1318, 2013.

Gardner, A. S., Moholdt, G., Scambos, T., Fahnstock, M., Ligtenberg, S., van den Broeke, M., and Nilsson, J.: Increased West Antarctic ice discharge and East Antarctic stability over the last seven years, The Cryosphere Discuss., 2017, 1-39, 2017.

Geuzaine, C. and Remacle, J. F.: Gmsh: A 3‐D finite element mesh generator with built‐in pre‐ and post‐processing facilities, International Journal for Numerical Methods in Engineering, 79, 1309-1331, 2009.

Gillet-Chaulet, F., Durand, G., Gagliardini, O., Mosbeux, C., Mouginot, J., Rémy, F., and Ritz, C.: Assimilation of surface velocities acquired between 1996 and 2010 to constrain the form of the basal friction law under Pine Island Glacier, Geophysical Research Letters, doi: 10.1002/2016GL069937, 2016. n/a-n/a, 2016.

Gillet-Chaulet, F., Gagliardini, O., Seddik, H., Nodet, M., Durand, G., Ritz, C., Zwinger, T., Greve, R., and Vaughan, D. G.: Greenland ice sheet contribution to sea-level rise from a new-generation ice-sheet model, The Cryosphere, 6, 1561-1576, 2012.

Gladstone, R., Schäfer, M., Zwinger, T., Gong, Y., Strozzi, T., Mottram, R., Boberg, F., and Moore, J. C.: Importance of basal processes in simulations of a surging Svalbard outlet glacier, The Cryosphere, 8, 1393-1405, 2014.

Glen, J. W.: The creep of polycrystalline ice, 1955, 519-538.

Gong, Y., Zwinger, T., Cornford, S., Gladstone, R., SchÄFer, M., and Moore, J. C.: Importance of basal boundary conditions in transient simulations: case study of a surging marine-terminating glacier on Austfonna, Svalbard, Journal of Glaciology, doi: 10.1017/jog.2016.121, 2016. 1-12, 2016.

Hansen, P. C.: The L-curve and its use in the numerical treatment of inverse problems, Computational inverse problems in electrocardiology, 5, 2001.

Korona, J., Berthier, E., Bernard, M., Rémy, F., and Thouvenot, E.: SPIRIT. SPOT 5 stereoscopic survey of Polar Ice: Reference Images and Topographies during the fourth International Polar Year (2007–2009), ISPRS Journal of Photogrammetry and Remote Sensing, 64, 204-212, 2009.

Lemoine, F. G., Kenyon, S. C., Factor, J. K., Trimmer, R. G., Pavlis, N. K., Chinn, D. S., Cox, C. M., Klosko, S. M., Luthcke, S. B., and Torrence, M. H.: The development of the joint NASA GSFC and the National Imagery and Mapping Agency (NIMA) geopotential model EGM96, NASA Goddard Space Flight Center, Greenbelt, Maryland, 20771 USA, 1998. 1998.

MacAyeal, D. R.: A tutorial on the use of control methods in ice-sheet modeling, Journal of Glaciology, 39, 91-98, 1993.

Morlighem, M., Rignot, E., Seroussi, H., Larour, E., Ben Dhia, H., and Aubry, D.: A mass conservation approach for mapping glacier ice thickness, Geophysical Research Letters, 38, n/a-n/a, 2011.

Morlighem, M., Rignot, E., Seroussi, H., Larour, E., Ben Dhia, H., and Aubry, D.: Spatial patterns of basal drag inferred using control methods from a full‐Stokes and simpler models for Pine Island Glacier, West Antarctica, Geophysical Research Letters, 37, 2010.

Morlighem, M., Seroussi, H., Larour, E., and Rignot, E.: Inversion of basal friction in Antarctica using exact and incomplete adjoints of a higher-order model, Journal of Geophysical Research: Earth Surface, 118, 1746-1753, 2013.

Mouginot, J., Rignot, E., and Scheuchl, B.: Sustained increase in ice discharge from the Amundsen Sea Embayment, West Antarctica, from 1973 to 2013, Geophysical Research Letters, 41, 1576-1584, 2014.

Rignot, E., Mouginot, J., and Scheuchl, B.: Antarctic grounding line mapping from differential satellite radar interferometry, Geophysical Research Letters, 38, L10504, 2011a.

Rignot, E., Mouginot, J., and Scheuchl, B.: MEaSUREs InSAR-Based Antarctica Ice Velocity Map [Version1.0], Boulder, Colorado USA: NASA DAAC at the National Snow and Ice Data Center., doi: 10.5067/MEASURES/CRYOSPHERE/nsidc-0484.001, 2011b. 2011b.

Schäfer, M., Gillet-Chaulet, F., Gladstone, R., Pettersson, R., A. Pohjola, V., Strozzi, T., and Zwinger, T.: Assessment of heat sources on the control of fast flow of Vestfonna ice cap, Svalbard, The Cryosphere, 8, 1951-1973, 2014.

Schäfer, M., Zwinger, T., Christoffersen, P., Gillet-Chaulet, F., Laakso, K., Pettersson, R., Pohjola, V. A., Strozzi, T., and Moore, J. C.: Sensitivity of basal conditions in an inverse model: Vestfonna ice cap, Nordaustlandet/Svalbard, The Cryosphere, 6, 771-783, 2012.

Seroussi, H., Morlighem, M., Rignot, E., Khazendar, A., Larour, E., and Mouginot, J.: Dependence of century-scale projections of the Greenland ice sheet on its thermal regime. 2013.

van Wessem, J. M., Reijmer, C. H., Lenaerts, J. T. M., van de Berg, W. J., van den Broeke, M. R., and van Meijgaard, E.: Updated cloud physics in a regional atmospheric climate model improves the modelled surface energy balance of Antarctica, The Cryosphere, 8, 125-135, 2014.

Walker, C. C. and Gardner, A. S.: Rapid drawdown of Antarctica's Wordie Ice Shelf glaciers in response to ENSO/Southern Annular Mode-driven warming in the Southern Ocean, Earth and Planetary Science Letters, 476, 100-110, 2017.

Wendt, J., Rivera, A., Wendt, A., Bown, F., Zamora, R., Casassa, G., and Bravo, C.: Recent ice-surface-elevation changes of Fleming Glacier in response to the removal of the Wordie Ice Shelf, Antarctic Peninsula, Annals of Glaciology, 51, 97-102, 2010.

Wouters, B., Martin-Español, A., Helm, V., Flament, T., van Wessem, J. M., Ligtenberg, S. R. M., van den Broeke, M. R., and Bamber, J. L.: Dynamic thinning of glaciers on the Southern Antarctic Peninsula, Science, 348, 899-903, 2015.

The Cryosphere Discuss., https://doi.org/10.5194/tc-2017-241
Manuscript under review for journal The Cryosphere
Discussion started: 2 January 2018

Zhao, C., Gladstone, R., Zwinger, T., Warner, R., and King, M. A.: Basal drag of Fleming Glacier, Antarctica, Part 2: implications of evolution from 2008 to 2015, The Cryosphere, companion paper. companion paper.

Zhao, C., King, M. A., Watson, C. S., Barletta, V. R., Bordoni, A., Dell, M., and Whitehouse, P. L.: Rapid ice unloading in the Fleming Glacier region, southern Antarctic Peninsula, and its effect on bedrock uplift rates, Earth and Planetary Science Letters, 473, 164-176, 2017.

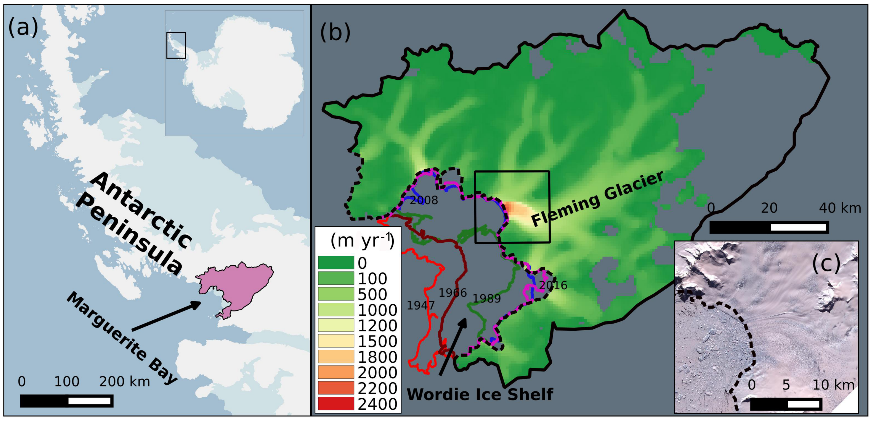

600

Figure 1. (a) The location of the Wordie Ice Shelf-Fleming Glacier system in the Antarctica Peninsula (pink polygon). (b) Surface speed in 2008 with a spatial resolution of 900 m obtained from InSAR data (Rignot et al., 2011b) for the study regions. Colored lines represent the ice front position in 1947 (red), 1966 (brown), 1989 (green), 2008 (blue), and 2016
605 (magenta) obtained from Cook and Vaughan (2010), Wendt et al. (2010), and Zhao et al. (2017). The grey area inside the catchment shows the region without velocity data. (c) Ice front images acquired from ASTER L1T data on Feb 2nd, 2009.

The Cryosphere Discuss., https://doi.org/10.5194/tc-2017-241
Manuscript under review for journal The Cryosphere
Discussion started: 2 January 2018

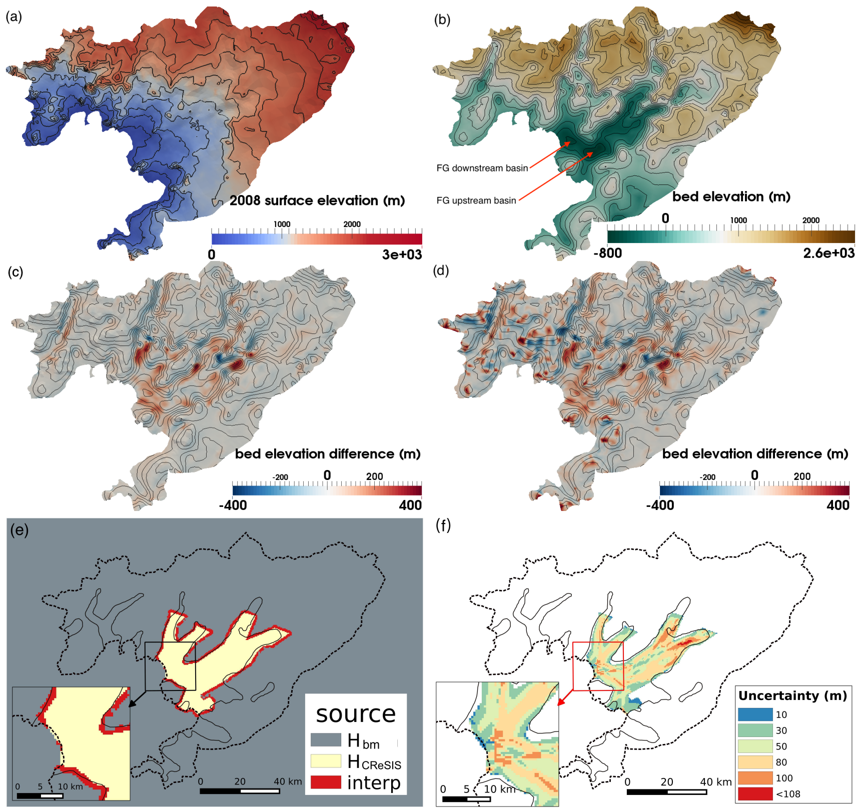

610

Figure 2. (a) Surface elevation data in 2008 with black contours (interval: 200 m) representing the surface elevation. (b) bed elevation data from bed_bm, (c) elevation difference between bed_mc and bed_bm (d) elevation difference between bed_zc and bed_bm. The black contours in (b-d) show the bed elevation with an interval of 200 m. (e) The ice thickness data sources and (f) the uncertainty of the ice thickness data H_{mc} with black solid lines representing
615 the observed ice surface velocity of 100 m yr^{-1}.

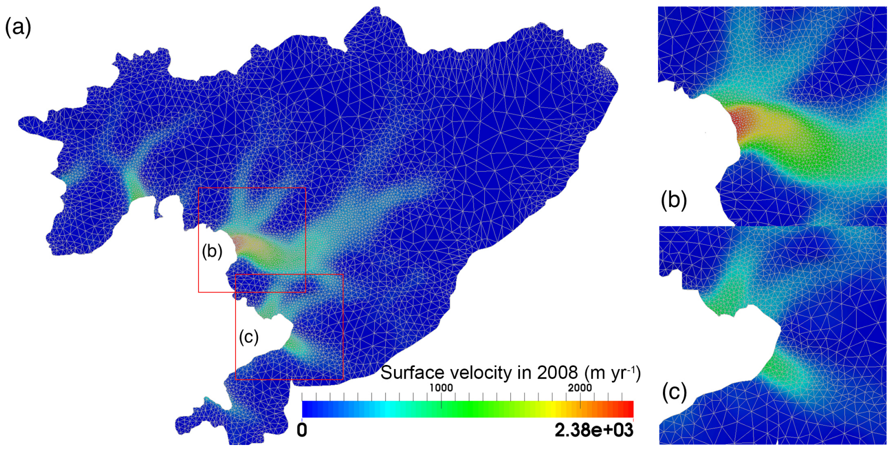

Figure 3. (a) Mesh structure of the domain in the current study with surface velocity in 2008 (Rignot et al., 2011b) and the zoomed-in map for (b) the Fleming Glacier and (c) the Prospect
620 Glacier.

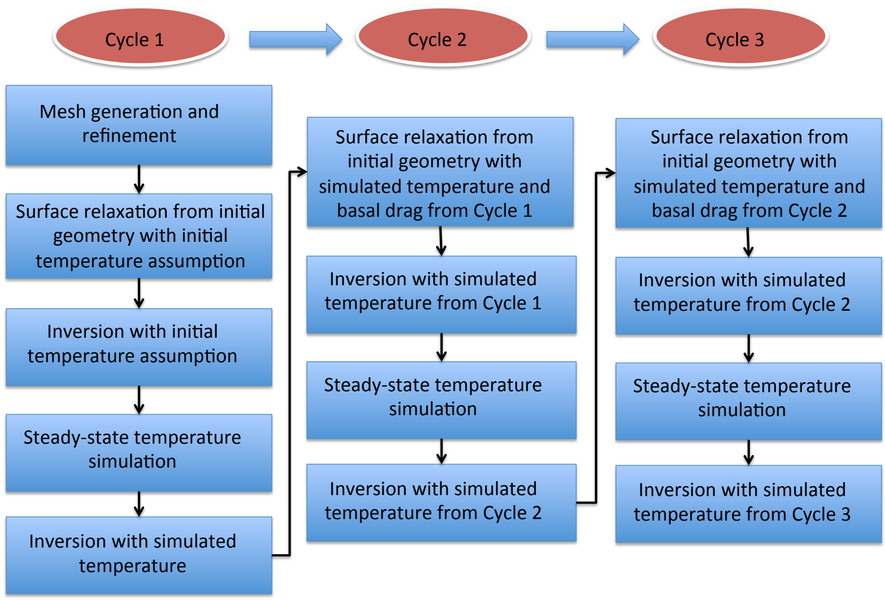

Figure 4. Flow chart of simulation spin-up with three cycles.

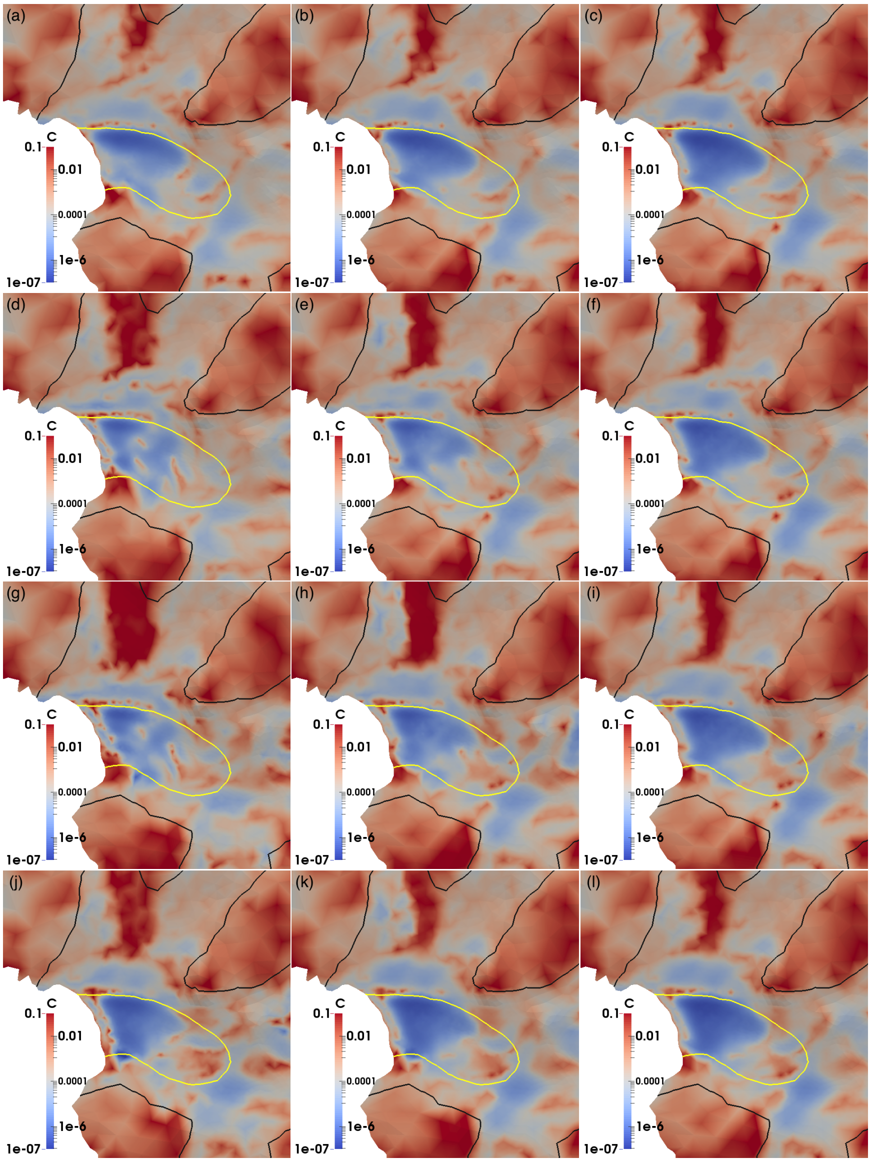

625

Figure 5. Basal drag coefficient ***C*** (MPa m^{-1} yr) inferred from experiments: (a-c) TEMP1, (d-f) TEMP2, (g-i) CONTROL, and (j-l) TEMP4. The left (a, d, g, j), middle (b, e, h, k) and right
630 columns (c, f, i, l) are the inferred basal drag coefficients from Cycle 1, Cycle 2 and Cycle 3, respectively. The black and yellow solid lines represent observed surface speed contours of 100 m yr^{-1} and 1000 m yr^{-1}, respectively.

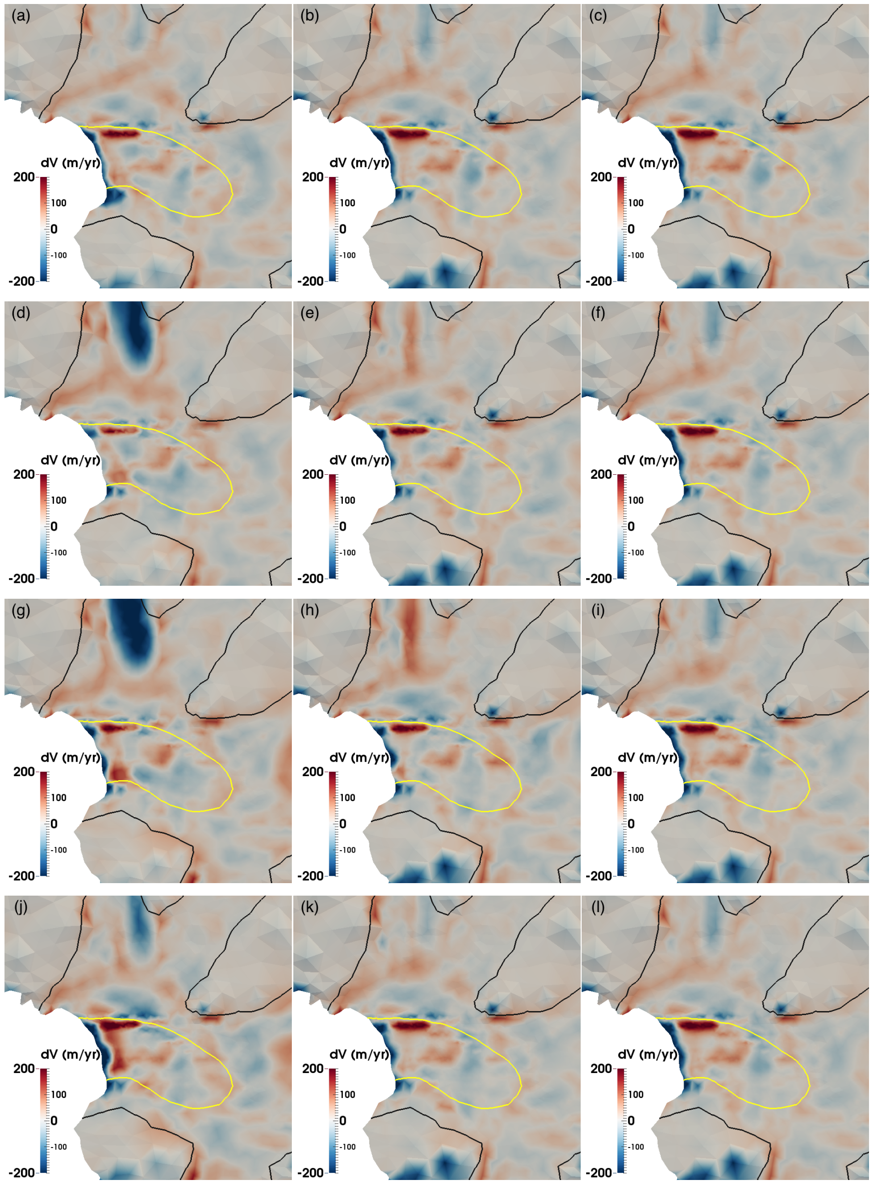

Figure 6. Mismatch between the observed and simulated surface speed in 2008 (observed minus simulated) from experiments: (a-c) TEMP1, (d-f) TEMP2, (g-i) CONTROL, and (j-l) TEMP3. The left (a, d, g, j), middle (b, e, h, k) and right columns (c, f, i, l) are the inferred basal drag coefficients from Cycle 1, Cycle 2 and Cycle 3, respectively. The black and yellow solid lines represent observed surface speed contours of 100 m yr^{-1} and 1000 m yr^{-1}, respectively.

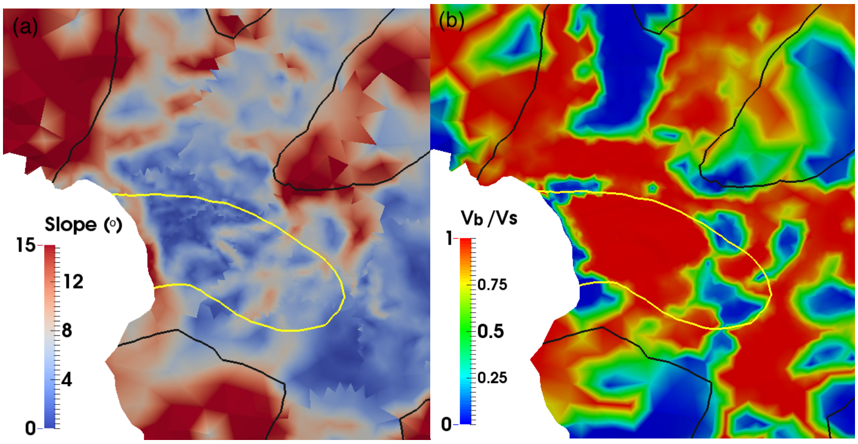

645

Figure 7. (a) The slope (degree) of the relaxed surface and (b) the ratio of magnitude of the modeled basal and surface velocity (basal over surface) after three-cycle spin-up scheme from experiment: CONTROL. The maximum difference around the ice front is ~2600 m yr^{-1}. The zigzag discontinuities in (a) are artefacts of the post-processing at partition boundaries only, and do not affect the simulations. The black and yellow solid lines represent surface speed contours of 100 m yr^{-1} and 1000 m yr^{-1}, respectively.

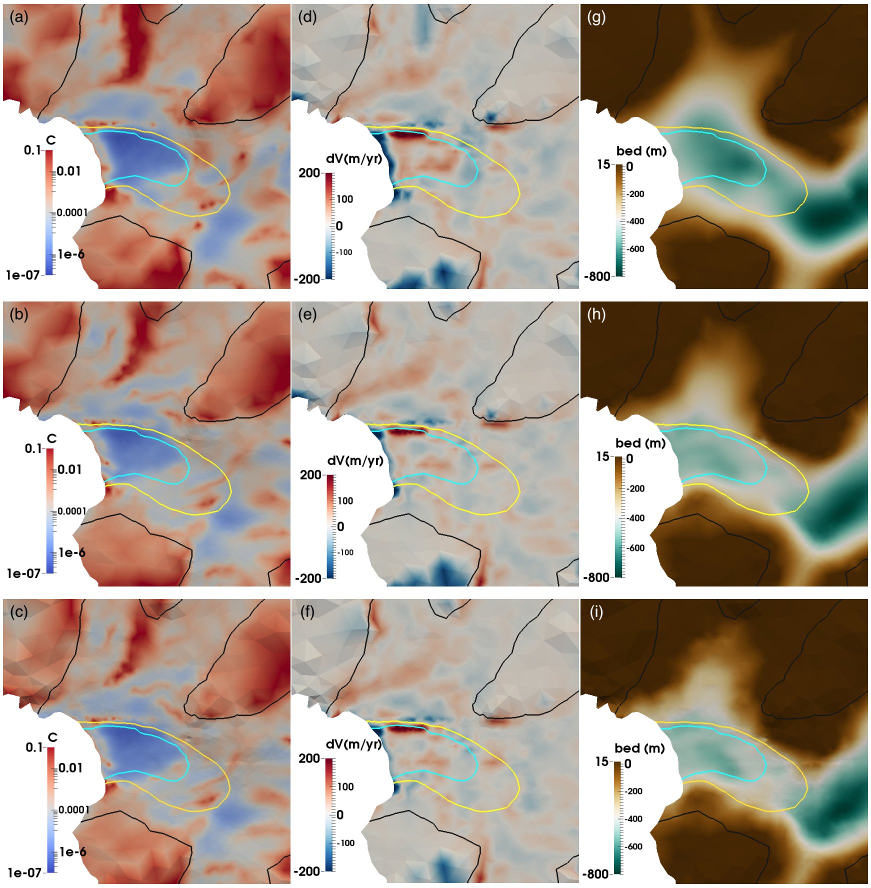

Figure 8. Distribution of basal friction coefficient ***C*** (MPa m^{-1} yr) (left column) and mismatch between the observed and modeled surface velocity (observed minus simulated; middle column) from experiments: (a, d) CONTROL, (b, e) BEDMC, and (c, f) BEDZC with bedrock data from (g) bed_bm; (h) bed_mc; (i) bed_zc, respectively. The black, yellow, and cyan solid lines represent observed surface speed contours of 100 m yr^{-1}, 1000 m yr^{-1} and 1500 m yr^{-1}, respectively.

The Cryosphere Discuss., https://doi.org/10.5194/tc-2017-241
Manuscript under review for journal The Cryosphere
Discussion started: 2 January 2018

The Cryosphere
Discussions
Open Access

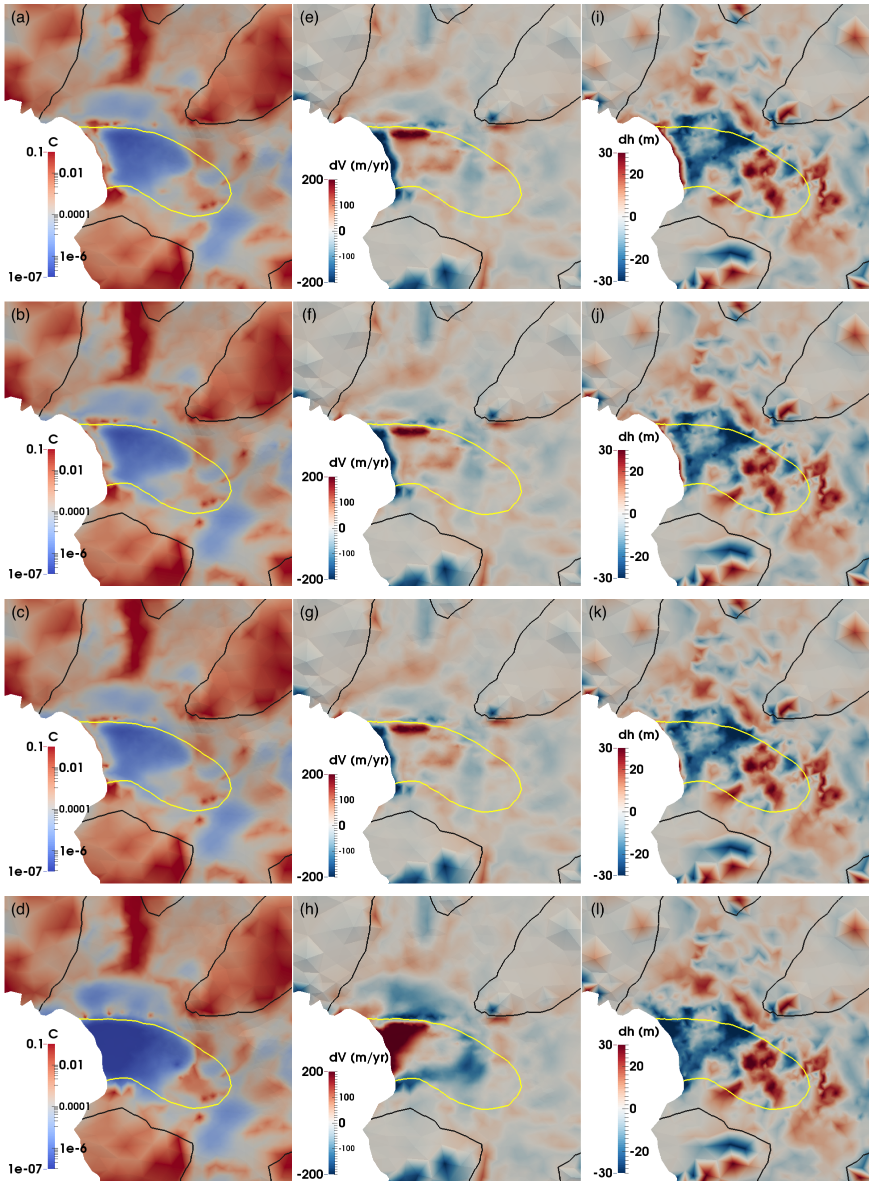

Figure 9. Left column: Distribution of basal friction coefficient C (MPa m^{-1} yr) inferred from experiments: (a) IFBC1, (b) CONTROL, (c) IFBC2, and (d) IFBC3. Middle column: the mismatch between the observed and modeled surface velocity (observed minus simulated) from experiments: (e) IFBC1, (f) CONTROL, (g) IFBC2, and (h) IFBC3. The right column: the difference between the observed initial surface and relaxed surface elevation (observed minus relaxed) from experiments: (i) IFBC1, (j) CONTROL, (k) IFBC2, and (l) IFBC3. The black and yellow solid lines represent surface speed contours of 100 m yr^{-1} and 1000 m yr^{-1}, respectively.

The Cryosphere Discuss., https://doi.org/10.5194/tc-2017-241
Manuscript under review for journal The Cryosphere
Discussion started: 2 January 2018

The Cryosphere Discussions
Open Access
EGU

Table 1. List of parameter values used in this study.

Parameters	Symbol	Values	Units
Enhancement Factor	E	2.5	
Rheological parameter in the Arrhenius law	A_0 (T < -10 ℃)	3.985×10^{-13}	$Pa^{-3}\ s^{-1}$
	A_0 (T > -10 ℃)	1.916×10^{3}	$Pa^{-3}\ s^{-1}$
Activation energy in the Arrhenius law	Q_0 (T < -10 ℃)	-60	$kJ\ mol^{-1}$
	Q_0 (T > -10 ℃)	-139	$kJ\ mol^{-1}$
Gravitational constant	g	9.8	$m\ s^{-2}$
Exponent of Glen flow law	n	3	
Density of ocean water	ρ_w	1025	$kg\ m^{-3}$
Density of ice	ρ_i	900	$kg\ m^{-3}$

Table 2 Experiment lists. n/a is short for "not applicable".

Experiment	Description	Bed topography used	Initial temperature in surface relaxation of Cycle 1	Initial temperature in first inversion of Cycle 1	Sea level used
CONTROL	Spin-up for three cycles with initial linear temperature	bed_bm	Linear temperature	Linear temperature	15 m
TEMP1	Spin-up for three cycles with initial constant temperature of -20 ℃	bed_bm	-20 ℃	-20 ℃	15 m
TEMP2	Spin-up for three cycles with initial constant temperature of -5 ℃	bed_bm	-5 ℃	-5 ℃	15 m
TEMP3	Spin-up for three cycles with initial linear temperature for surface relaxation but a constant temperature -20 ℃ of for the first inversion	bed_bm	-20 ℃	Linear temperature	15 m
BEDZC	Spin-up for three cycles with bed_zc as the bed topography	bed_zc	Linear temperature	Linear temperature	15 m
BEDMC	Spin-up for three cycles with bed_mc as the bed topography	bed_mc	Linear temperature	Linear temperature	15 m
IFBC1	Spin-up for three cycles with low ice front pressure	bed_bm	Linear temperature	Linear temperature	5 m
IFBC2	Spin-up for three cycles with high ice front pressure	bed_bm	Linear temperature	Linear temperature	25 m
IFBC3	Spin-up for three cycles with extreme ice front pressure	bed_bm	Linear temperature	Linear temperature	n/a